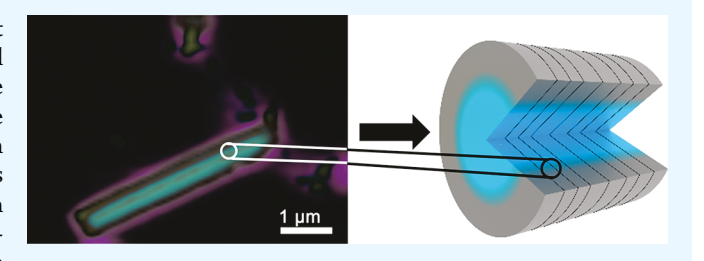
# Roadblocks in Cation Diffusion Pathways: Implications of Phase Boundaries for Li-Ion Diffusivity in an Intercalation Cathode Material

Yuting Luo,<sup>†</sup> Luis R. De Jesus,<sup>†</sup> Justin L. Andrews,<sup>†</sup> Abhishek Parija,<sup>†</sup> Nathan Fleer,<sup>†</sup> Daniel Juarez Robles,<sup>‡</sup> Partha P. Mukherjee,\*,<sup>‡</sup> and Sarbajit Banerjee\*,<sup>†</sup>

Supporting Information

ABSTRACT: Increasing intercalation of Li-ions brings about distortive structural transformations in several canonical intercalation hosts. Such phase transformations require the energy dissipative creation and motion of dislocations at the interface between the parent lattice and the nucleated Li-rich phase. Phase inhomogeneities within particles and across electrodes give rise to pronounced stress gradients, which can result in capacity fading. How such transformations alter Liion diffusivities remains much less explored. In this article, we



use layered V<sub>2</sub>O<sub>5</sub> as an intercalation host and examine the structural origins of the evolution of Li-ion diffusivities with phase progression upon electrochemical lithiation. Galvanostatic intermittent titration measurements show a greater than 4 orders of magnitude alteration of Li-ion diffusivity in  $V_2O_5$  as a function of the extent of lithiation. Pronounced dips in Li-ion diffusivities are correlated with the presence of phase mixtures as determined by Raman spectroscopy and X-ray diffraction, whereas monophasic regimes correspond to the highest Li-ion diffusivity values measured within this range. First-principles density functional theory calculations confirm that the variations in Li-ion diffusivity do not stem from intrinsic differences in diffusion pathways across the different lithiated V2O5 phases, which despite differences in the local coordination environments of Li-ions show comparable migration barriers. Scanning transmission X-ray microscopy measurements indicate the stabilization of distinct domains reflecting the phase coexistence of multiple lithiated phases within individual actively intercalating particles. The results thus provide fundamental insight into the considerable ion transport penalties incurred as a result of phase boundaries formed within actively intercalating particles. The combination of electrochemical studies with ensemble structural characterization and single-particle X-ray imaging of phase boundaries demonstrates the profound impact of interfacial phenomena on macroscopic electrode properties.

KEYWORDS: Li-ion batteries, cathode materials, kinetic behavior, phase transformations, phase boundaries, inhomogeneities, diffusivities, vanadium oxides

## 1. INTRODUCTION

Li-ion batteries have rapidly eclipsed competing alternatives in terms of powering consumer electronics and are on a promising trajectory for large-area applications such as grid-level storage. 1-3 Despite their immense potential, intercalation batteries are plagued by a number of limitations spanning the range from loss of capacity upon extended cycling to inadequate high-rate performance and a dearth of electrode materials that can deliver a combination of high voltage and high capacity. 4-6 The thermodynamic driving forces (determined by the freeenergy differential for Li-ions between the cathode and anode material) and kinetics of cation diffusion (governed by atomistic and interfacial migration barriers) determine the energy and power density that can be viably extracted from the battery.<sup>4</sup> Atomistic modeling of diffusion pathways of intercalated cations within crystalline lattices is commonly used as a means of evaluating the magnitude of migration barriers for atomistic

hopping events. 5,6 However, low values of migration barriers in such calculations represent a necessary but not sufficient condition for a viable cathode material because cation diffusion realistically occurs not just along well-defined atomistic diffusion pathways, but also across the entire span of mesoscopic porous electrode architectures encompassing grain boundaries and interfaces between particles. <sup>7–10</sup> In many intercalation hosts, Liion insertion induces distortive structural phase transitions. In such materials, during the discharge process, the Li-rich phase must be nucleated and propagated across individual particles as a result of supersaturation with lithium. The implications of the resulting phase boundaries stabilized within actively intercalating particles for Li-ion diffusivity remain to be well understood.<sup>4</sup>

Received: June 25, 2018 Accepted: August 14, 2018 Published: August 14, 2018



Department of Chemistry, Department of Materials Science & Engineering, Texas A&M University, College Station, Texas 77843,

<sup>\*</sup>School of Mechanical Engineering, Purdue University, West Lafayette, Indiana 47907, United States

In this article, using layered V<sub>2</sub>O<sub>5</sub> as a model intercalation host, we use galvanostatic intermittent titration methods in conjunction with structural characterization of lithiated phases and X-ray microscopy imaging of phase boundaries within individual electrode particles to elucidate the influence of phase segregation on Li-ion diffusivity.

In many classical intercalation hosts, increasing the concentration of intercalated Li-ions brings about a structural transformation in order to reduce cationic repulsions, accommodate crystallographic site preferences of reduced transition metals, and allow for better screening of the increased electron density. Such phase transformations, which are accompanied by significant distortion of crystalline frameworks, must accommodate the lattice distortions through creation and motion of dislocations at the interface between the parent lattice and the nucleated Li-rich phase. As entropy-producing energydissipative processes, such transformations oftentimes underpin hysteresis and give rise to considerable inhomogeneities across the porous electrode. The nucleation and propagation of phase transformations across space and time are strongly dependent on the particle morphology, crystallite dimensions, nature of interconnects between particles, connectivity to the current collector, and the local overpotential. 11-14 Increasing evidence points to spatiotemporal phase propagation being dictated by local reactivity and lithiation gradients rather than the global voltage profile. 14-16

Orthorhombic vanadium pentoxide  $(V_2O_5)$  is a canonical intercalation host characterized by an alternating up-up-downdown arrangement of  $[VO_5]$  square pyramids with edge- and corner-sharing oxygens. <sup>17,18</sup> In principle, it can accommodate as many as 3 Li-ions per formula unit (corresponding to a theoretical specific capacity of 442 mA h/g) through a series of structural rearrangements, albeit the viable extent of reversible intercalation is much lower. 19,20 V<sub>2</sub>O<sub>5</sub> serves as an excellent model system for evaluating the influence of phase transformations and segregation on Li-ion diffusivity because Li-ion intercalation brings about very many such transitions across different concentration windows (denoted as x in  $Li_xV_2O_5$ ). As observed with other intercalation hosts, the spatiotemporal dynamics of phase nucleation and propagation are strongly influenced by particle size and connectivity within this system. 10,21,22' Below a critical size, phase boundaries can no longer be stabilized within particles, and thus phase nucleation and growth is instead supplanted by insertion of Li-ions through a solid-solution mechanism.<sup>23</sup> Recent chemical imaging of lithiated V<sub>2</sub>O<sub>5</sub> nanowires suggests intriguing charge striping of Li-rich and Li-poor domains along the length of the nanowires. 15 The rich multiphasic behavior and clear delineation of phasesegregated domains within individual particles of V2O5 make it an excellent model system for probing the influence of phase boundaries on Li-ion diffusivity. In this article, the galvanostatic intermittent titration technique (GITT) has been used to probe the diffusivity of Li-ions in voltage windows corresponding to different depths of discharge. In their foundational work on GITT, Weppner and Huggins extracted kinetic parameters of Li<sub>3</sub>Sb as an electrode.<sup>24</sup> Since then, GITT has been widely applied to evaluate the kinetic parameters of cathode materials with LiNi<sub>x</sub>Mn<sub>y</sub>Co<sub>z</sub>O<sub>2</sub> and LiFePO<sub>4</sub> being two prominent examples. <sup>25-29</sup> Zhu and Wang have combined GITT with potentiostatic intermittent titration technique measurements to describe the coupling between ion diffusion and interface migration in the  $\alpha$ - and  $\beta$ -phases of Li<sub>x</sub>FePO<sub>4</sub>. Their work suggests that in phase-transforming materials, strain accommodation at interfaces influences the mobility of interfaces and strongly impacts the diffusion of ions between two phases. Here, we seek to correlate measured Li-ion diffusivities extracted from GITT to phase segregation evidenced by powder X-ray diffraction (XRD), Raman microprobe analysis, and scanning transmission X-ray microscopy (STXM). The results provide fundamental insight into the considerable ion transport resistance that arises from phase boundaries stabilized within actively intercalating particles.

#### 2. MATERIALS AND METHODS

- 2.1. Synthesis of V<sub>2</sub>O<sub>5</sub> Nanowires. Single-crystalline V<sub>2</sub>O<sub>5</sub> nanowires were grown using hydrothermal methods as reported in a previous work.<sup>22</sup> In brief, V<sub>2</sub>O<sub>5</sub> nanowires were synthesized by the air oxidation (350 °C, 48 h) of V<sub>3</sub>O<sub>7</sub>·H<sub>2</sub>O nanowires, which in turn were prepared by the hydrothermal reduction of bulk V<sub>2</sub>O<sub>5</sub> by oxalic acid (210 °C, 72 h).
- 2.2. Cyclic Voltammetry (CV), Galvanostatic Discharge, and GITT Measurements. Coin cells were assembled in an argon-filled glovebox for electrochemical testing. The working electrode was fabricated by casting the mixture of the active material (V2O5 nanowires, 70 wt %), conductive carbon [Super C65 (MTI Corporation), 20 wt %], and binder [poly(vinylidene fluoride), 10 wt %] dispersed in N-methyl-2-pyrrolidone onto an Al foil substrate. The reference electrode is Li metal (Sigma-Aldrich). The electrolyte used was a 1.0 M solution of LiPF<sub>6</sub> in a [1:1 (v/v)] mixture of diethyl carbonate and ethylene carbonate (Sigma-Aldrich). Galvanostatic measurements were performed by using a LANHE battery testing system (CT2001A) at a 0.05 C rate at room temperature during charge/discharge cycling. CV measurements were performed at a scan rate of 0.1 mV/s using a Bio-Logic electrochemical workstation across the charge/discharge process. GITT measurements were performed in the voltage window between 1.00 and 4.00 V by using a LANHE battery testing system (CT2001A). The cell was discharged at a 0.05 C rate for 10 min with a 20 min relaxation time between each flux.
- 2.3. Computational Details. The diffusion pathways and energetics of diffusion of Li-ions in lithiated phases of V2O5 were determined based on density functional theory (DFT) calculations using the nudged elastic band (NEB) method as implemented in the Vienna ab initio simulation package. 30,31 The projector-augmented wave formalism was used to describe the electron-ion interactions. The Perdew-Burke-Ernzerhof formulation of the generalized gradient approximation to the exchange-correlation potential was used to include the electronic exchange and correlation effects.<sup>32</sup> A total of 7 images for  $\alpha$ -Li<sub>0.083</sub>V<sub>2</sub>O<sub>5</sub> and  $\varepsilon$ -Li<sub>0.330</sub>V<sub>2</sub>O<sub>5</sub>, and 11 images for  $\delta$ - $\rm Li_{0.917}V_2O_5$  and  $\gamma\text{-Li}_{1.083}V_2O_5$  were interpolated between the initial and final positions to describe the diffusion of the ions. The end positions and the images for the NEB path were optimized to a force tolerance of  $\pm 0.05$  eV Å<sup>-1</sup>. To avoid physically unreasonable interactions, supercells of adequate dimensions were used such that the distance between the images was no less than 9.1 Å. In the energy barrier calculations, a Monkhorst-Pack reciprocal space grid of  $2 \times 2 \times 2$  k-points for the supercells was used for numerical sampling of the first Brillouin zone.
- **2.4. Electron Microscopy.** Scanning electron microscopy (SEM) was performed using a JEOL JSM-7500F field-emission scanning electron microscope operated at an accelerating voltage of 5 kV. Samples were prepared for SEM by dispersing powders onto carbon tape. High-resolution transmission electron microscopy (TEM) images were acquired using an FEI Tecnai G2 F20 ST instrument. Briefly, samples were dispersed in 2-propanol followed by drop-casting onto 400-mesh holey-carbon films supported by copper grids (Electron Microscopy Science, Hatfield, PA). Sample-loaded grids were dried in air at room temperature. The Tecnai was operated at an accelerating voltage of 200 kV.

Powder XRD. The Al foil current collectors from disassembled coin cells were washed with copious amounts of hexanes in an argon-filled glovebox. Next, the electrodes were affixed onto silicon holders for powder XRD measurements. XRD patterns were collected in Bragg-Brentano geometry using a Bruker D-8 Discovery diffractometer

equipped with a Lynxeye detector (25 kV, 40 mA). Rietveld analysis was performed to extract relative compositions of the lithiated phases using the EXPGUI interface in the GSAS software suite.33 Lattice parameters, profile terms, and vanadium positions were refined.<sup>34–37</sup> For discharged samples exhibiting a phase mixture, the scaling factor (S) refined during Rietveld analysis of the obtained diffraction patterns was used for quantitative evaluation of the fractional proportion of each phase. Because the densities of the unit cells can be determined based on the refined lattice parameters and composition, the scaling factor can be computed and extrapolated to a weight fraction.<sup>38</sup> The weight fractions for multiple phases were computed using the refined phase scaling correction  $(S_{\alpha})$ , which is related to the weight phase fractions as

$$W_{\alpha} = \frac{S_{\alpha} m_{\alpha}}{\sum_{\alpha=1}^{N_{\alpha}} S_{\alpha} m_{\alpha}} \tag{1}$$

where *m* is the unit cell mass (which is deduced from the refinement); the subscript  $\alpha$  denotes the specific phase; and  $S_{\alpha}$  is the scale factor computed for each phase. A more detailed derivation of eq 1, including its direct relation to the integrated intensity, intensity correction factors, form factors, and volume fractions can be found elsewhere.<sup>38</sup> structures depicted in the displayed figures were rendered using the VESTA software suite.3

**2.5. Raman Spectroscopy.** Raman spectra were acquired using an MPLN 100× microscope coupled with a Jobin-Yvon HORIBA Labram HR instrument. The 514.5 nm line from an Ar-ion laser was used as the

2.6. Scanning Transmission X-ray Microscopy. STXM data were collected at the spectromicroscopy beamline 10ID-1 of the Canadian Light Source, Saskatoon, SK. The beamline is equipped with an elliptically polarized undulator source. Incident soft X-rays in the energy range 508-560 eV were focused onto the sample of interest using a Fresnel zone-plate, which includes an order-sorting aperture to eliminate undesired diffraction orders. A plane grating monochromator with 500 line  $\mbox{mm}^{-1}$  was used for hyperspectral imaging at V L- and O Kedges. A dwell time of 1 ms was used for signal acquisition at each pixel. The image stacks were analyzed using aXis2000 (http://unicorn. mcmaster.ca/aXis2000.html). Region-of-interest (ROI) maps were obtained by singular value decomposition (SVD) of the image stack, and by using as a reference, spectral components identified within different regions of the stack as noted in previous work. 10 This procedure yields a set of spatially resolved composition maps where intensities represent the pixel-wise signal strength of each of the selected components.

# 3. RESULTS AND DISCUSSION

3.1. Measurements of Li-lon Diffusivity in Electrochemically Lithiated V<sub>2</sub>O<sub>5</sub>. V<sub>2</sub>O<sub>5</sub> nanowires have been prepared by the air oxidation of V<sub>3</sub>O<sub>7</sub>·H<sub>2</sub>O nanowires as described in a previous work. 22 The nanowires are ca. 150–200 nm in diameter and span tens of microns in length as observed in the SEM image shown in Figure 1a. The TEM images and selected area electron diffraction (SAED) patterns in Figure 1 attest to the uniform morphology, faceted rectangular crosssections, and single-crystalline nature of the nanowires. The interplanar separations of 1.84 and 2.53 Å discernible in the lattice-resolved TEM image of Figure 1c can be assigned to the separations between the (112) and (211) planes of orthorhombic V<sub>2</sub>O<sub>5</sub>, respectively.

In order to elucidate the influence of structural transformations between crystalline phases on Li-ion diffusivity across a large voltage window, we have focused on early discharge/charge cycles. As such, the observed alterations in diffusivity (vide infra) can be ascribed to structural alterations of the intercalation host instead of stochastic defects inevitable upon prolonged cycling. 10,40,41 Figure 2 shows the electro-

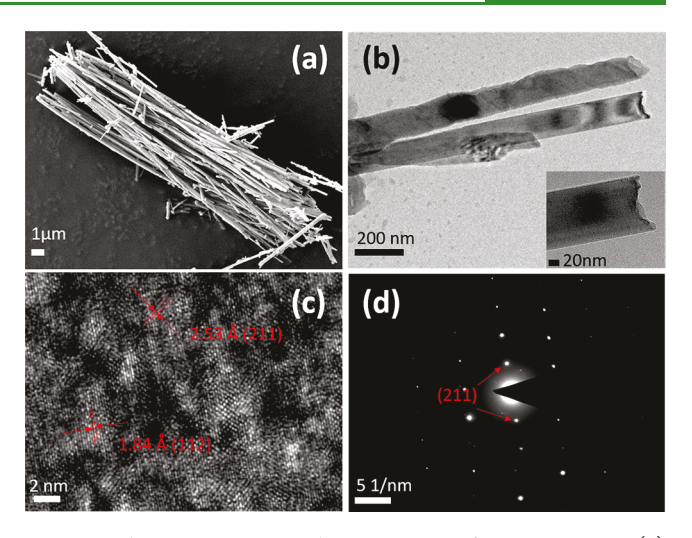


**Figure 1.** Electron microscopy characterization of V<sub>2</sub>O<sub>5</sub> nanowires. (a) SEM image, (b) low-magnification TEM image, (c) lattice-resolved TEM-image, and (d) SAED pattern of V<sub>2</sub>O<sub>5</sub> nanowires.

chemical characterization of V<sub>2</sub>O<sub>5</sub>. Figure 2a shows plots of the galvanostatic discharge/charge profile of V2O5 for three cycles in the voltage window between 2.00 and 4.00 V. The intercalationinduced structural transformations between the lithiated phases of V<sub>2</sub>O<sub>5</sub> can be observed as plateaus at 3.39, 3.20, and 2.37 V, corresponding to  $\alpha \to \varepsilon$ ,  $\varepsilon \to \delta$ , and  $\delta \to \gamma$  transformations, respectively; each of the plateaus thus reflects the coexistence of the end members with their relative proportion, reflecting the progression of the nucleation and growth of the Li-rich phase. A final plateau observed at 2.06 V corresponds to the transformation of  $\gamma$ -Li<sub>r</sub>V<sub>2</sub>O<sub>5</sub> to the highly disordered  $\omega$ -Li<sub>r</sub>V<sub>2</sub>O<sub>5</sub> phase. As shown in Figure 2c, the initial intercalation of Li ions (x < 0.1) brings about a homogeneous transformation to  $\alpha$ -Li<sub>x</sub>V<sub>2</sub>O<sub>5</sub>, allowing for almost complete retention of the structural morphology of the parent structure with only a slight increase of the interlayer separation along the c-axis to accommodate the inserted Li-ions. 18,42 With the increasing Li-ion concentration (0.35 < x < 0.7), the  $\varepsilon$ -Li<sub>x</sub>V<sub>2</sub>O<sub>5</sub> phase is stabilized; this structure is characterized by an increased interlayer separation along the caxis accompanied by puckering of the apical oxygens toward the Li-ions. <sup>18,43,44</sup> Further insertion of Li-ions stabilizes the  $\delta$ - $\text{Li}_x \text{V}_2 \text{O}_5$  phase between 0.88 < x < 1.0; this phase is characterized by highly puckered apical oxygens and sliding of the layers by half-a-unit-cell length along the b-axis to better accommodate the significantly increased concentration of Li-ions. 43,44 Beyond x > 1, Li<sub>x</sub>V<sub>2</sub>O<sub>5</sub> undergoes an irreversible transformation to stabilize the  $\gamma$ -Li<sub>x</sub>V<sub>2</sub>O<sub>5</sub> phase; a highly disordered  $\omega$ -Li<sub>x</sub>V<sub>2</sub>O<sub>5</sub> phase is stabilized at still higher Li-ion concentrations approaching  $x \approx 3.0^{.45}$  The irreversible transformation to  $\omega$ -Li<sub>x</sub>V<sub>2</sub>O<sub>5</sub> can be observed electrochemically in the charge curve for the first cycle, and indeed in subsequent discharge/charge cycles, the distinct plateaus reflective of phase transformations are no longer observed. Figure 2b further shows the results of CV measurements. The first discharge cycle (between 4.00 and 2.00 V) is characterized by four pronounced reduction peaks at 3.40, 3.21, 2.35, and 2.03 V (consistent with the plateaus observed in the galvanostatic discharge/charge profile). Similar to the galvanostatic charge/discharge measurements, the voltammograms show a diminution in intensities of the aforementioned peaks in subsequent cycles owing to the irreversible transformation to  $\omega$ -Li<sub>r</sub>V<sub>2</sub>O<sub>5</sub> within this voltage window.

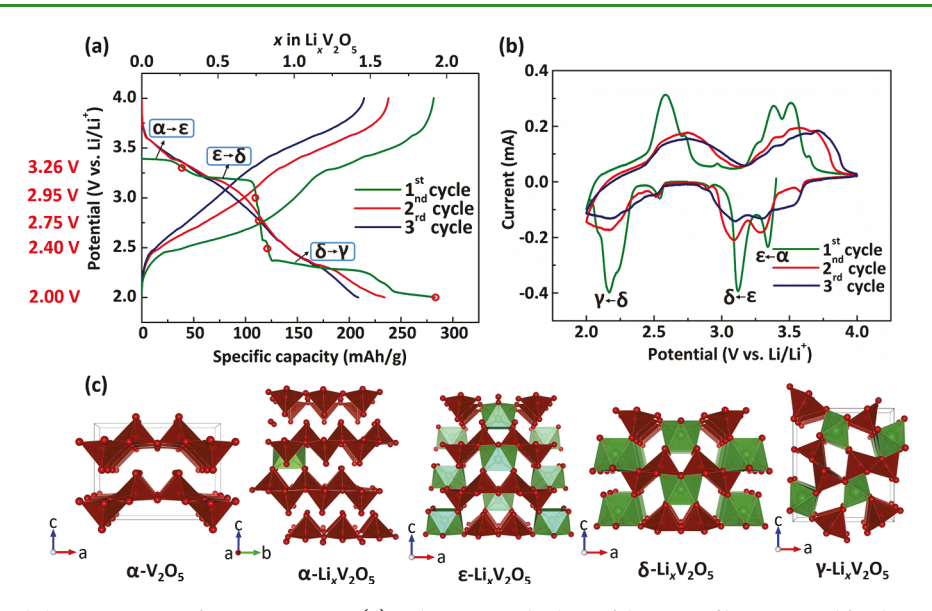


Figure 2. Electrochemical characterization of  $V_2O_5$  nanowires. (a) Galvanostatic discharge/charge profiles measured for three cycles at a C-rate of 0.05 C within a coin cell configuration. The red circles denote discharge voltages at which samples have been recovered for analysis by powder XRD and Raman microprobe analysis. (b) Cyclic voltammograms measured at a scan rate of 0.1 mV/s in the voltage range of 2.00 to 4.00 V vs Li/Li<sup>+</sup>. (c) Crystal structure renditions of α-V<sub>2</sub>O<sub>5</sub>, α-Li<sub>x</sub>V<sub>2</sub>O<sub>5</sub>, ε-Li<sub>x</sub>V<sub>2</sub>O<sub>5</sub>, δ-Li<sub>x</sub>V<sub>2</sub>O<sub>5</sub>, and γ-Li<sub>x</sub>V<sub>2</sub>O<sub>5</sub> indicating the sequence of intercalation-induced phase transformations.

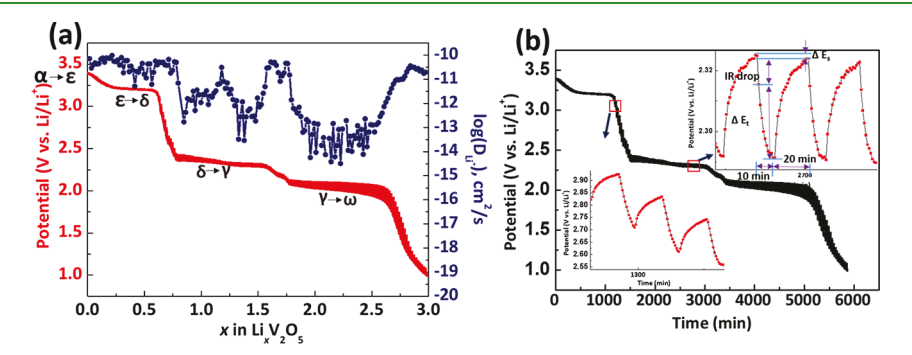


Figure 3. Measurements of Li-ion diffusivity in  $V_2O_5$ . (a) GITT measurements of  $V_2O_5$  nanowires in coin cells and extracted diffusion coefficient values plotted as a function of the Li-ion concentration (x) in  $\text{Li}_xV_2O_5$ . (b) Insets illustrate magnified views of the potential vs time profiles during monophasic Li-ion insertion and biphasic  $(\delta \to \gamma)$  intercalation-induced transformation segments. The cell is discharged at a 0.05 C rate for 10 min with a 20 min relaxation time between each flux.

The discharge profile and Li-ion diffusion coefficient values extracted from the GITT measurements are shown in Figure 3. The diffusion coefficient values have been measured for the first discharge curve of  $\text{Li}_{x}\text{V}_{2}\text{O}_{5}$  in the range of 1.00 to 4.00 V and are plotted as a function of the Li-ion concentration (x). As shown in Figure 3b and the insets depicting magnified views of the GITT plots, a gradual decrease of voltage between titrations corresponds to monophasic domains, whereas constant potential windows defining plateaus correspond to the occurrence of phase mixtures.<sup>6</sup> In the GITT measurement, the system is perturbed by imposing a constant current (I<sub>o</sub>) for a specific time interval  $(\tau)$ , while measuring the change in potential (E) as a function of time (t). By assuming constant diffusivity of the diffusing species in one direction and a semiinfinite solid, the evaluation of the surface concentration by Fick's equation with appropriate boundary conditions can be simplified in order to extract the diffusion coefficient  $(D_{Li})$  as per<sup>24,46</sup>

$$D_{\rm Li} = \frac{4}{\pi \tau} \left[ \frac{m_{\rm B} V_{\rm m}}{M_{\rm B} S} \right]^2 \left[ \frac{\Delta E_{\rm s}}{\Delta E_{\tau}} \right]^2 \qquad \text{when } \tau \ll h^2 / D_{\rm Li}$$
 (2)

where h is the maximum diffusion pathway,  $m_{\rm B}$  is the mass of the active material,  $M_{\rm B}$  is the atomic mass of the active material (181.88 g·mol<sup>-1</sup> for V<sub>2</sub>O<sub>5</sub>),  $V_{\rm m}$  is the molar volume of the compound (54.1 cm³·mol<sup>-1</sup>), S represents the geometric surface area of the electrode,  $\Delta E_{\rm s}$  indicates the change in the steady-state voltage of the cell at each applied galvanostatic current, and  $\Delta E_{\tau}$  is the measured change in the transient voltage of the cell during the step. <sup>46</sup> Measurements of Li-ion diffusivity in V<sub>2</sub>O<sub>5</sub> have been reported previously in the literature; <sup>19,20,24,25</sup> nevertheless, the origins of the modulation of diffusivity across the voltage window remain to be elucidated.

Figure 3 indicates that the Li-ion diffusivity values change nonmonotonically across 4 orders of magnitude from  $10^{-10}$  to  $10^{-14}\,\mathrm{cm^2\cdot s^{-1}}$  along the discharge curve. The logarithmic plot in Figure 3a indicates several pronounced dips as a function of the Li-ion concentration. At low Li-ion concentrations ( $x \le 0.3$ ),  $D_{\mathrm{Li}}$  values are in the range of ca.  $3\times10^{-11}$  to  $1\times10^{-10}$  cm $^2\cdot\mathrm{s^{-1}}$ . Interestingly, at ca. 3.37 V,  $D_{\mathrm{Li}}$  is slightly decreased to  $3\times10^{-11}$  cm $^2\cdot\mathrm{s^{-1}}$  corresponding to the nucleation of the  $\varepsilon$ -phase. Upon further discharge to ca. 3.20 V,  $D_{\mathrm{Li}}$  is reduced by 1 order of magnitude to ca.  $5\times10^{-12}\,\mathrm{cm^2\cdot s^{-1}}$ . With further progression of

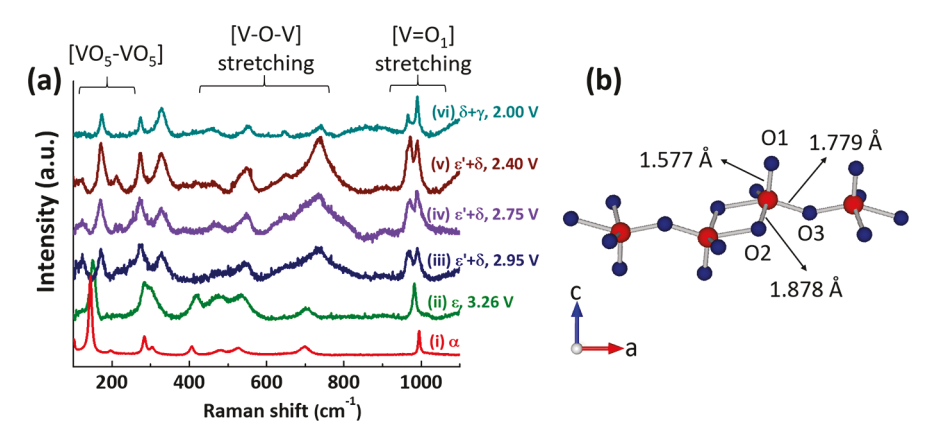


Figure 4. Raman spectroscopy analysis of phase mixtures in discharged samples. (a) Raman spectra acquired at 514.5 nm excitation for (i) unlithiated  $V_2O_5$  contrasted to spectra acquired for electrochemically discharged  $V_2O_5$  samples collected at (ii) 3.26; (iii) 2.95; (iv) 2.75; (v) 2.40; and (vi) 2.00 V. (b) Ball-and-stick depiction of vanadium local coordination and interconnectivity of  $V_2O_5$  square pyramids viewed along the crystallographic b axis.

Li-ion intercalation down to 2.40 V, corresponding to transformation of the  $\delta$ -phase to the highly distorted  $\gamma$ -phase,  $D_{\rm Li}$  is decreased from 5 × 10<sup>-11</sup> cm<sup>2</sup>·s<sup>-1</sup> to around 4 × 10<sup>-13</sup> cm<sup>2</sup>·s<sup>-1</sup>. In the voltage window of 2.30–2.10 V, corresponding to predominant stabilization of  $\gamma$ -Li<sub>x</sub>V<sub>2</sub>O<sub>5</sub>,  $D_{\rm Li}$  is substantially increased to ca. 10<sup>-11</sup> cm<sup>2</sup>·s<sup>-1</sup>. However, upon still further Li-ion insertion up to 2.00 V (corresponding to nucleation of the highly disordered  $\omega$ -phase of Li<sub>x</sub>V<sub>2</sub>O<sub>5</sub>),  $D_{\rm Li}$  is decreased by several orders of magnitude to ca. 10<sup>-14</sup> cm<sup>2</sup>·s<sup>-1</sup>. Finally, upon discharge down to 1.00 V, a  $D_{\rm Li}$  value of 10<sup>-11</sup> cm<sup>2</sup>·s<sup>-1</sup> is recovered. Remarkably, the reduction of  $D_{\rm Li}$  appears to be strongly correlated to discharge states corresponding to the initiation of a phase transformation or the coexistence of multiple phases. In contrast, the highest values of  $D_{\rm Li}$  (approaching ca. 10<sup>-10</sup> cm<sup>2</sup>·s<sup>-1</sup>) correspond to 3.34–3.25 V, 3.15–2.45 V, 2.30–2.10 V, and 1.95–1.00 V voltage windows, wherein the  $\varepsilon$ ,  $\delta$ ,  $\gamma$ , and  $\omega$  phases of Li<sub>x</sub>V<sub>2</sub>O<sub>5</sub> are expected to predominate (vide infra).

3.2. Structural Origins of Changes in Li-Ion Diffusivity. In order to uncover the origins of the observed modulation of Liion diffusivity, detailed ensemble and single-particle characterization has been performed for samples recovered from disassembled coin cells upon first discharge to 3.26, 2.95, 2.75, 2.40, and 2.00 V. Using Raman microprobe analysis and powder XRD measurements, the phase evolution of the materials has been examined as a function of the Li-ion concentration. In order to contrast potential differences in intrinsic Li-ion diffusivity arising from variations in the crystal structure as a result of intercalation-induced structural transformations, the NEB method has further been used to contrast the migration barriers for Li-ion diffusion in each of the phases. Finally, in order to distinguish between scenarios wherein the electrode comprises particles individually of different phases from an alternative scenario wherein phase separation occurs within individual particles, STXM measurements have been performed to delineate phase segregation at the single-particle level.

Raman spectroscopy studies of discharged samples (Figure 4) provide a means of distinguishing different lithiated phases of  $V_2O_5$  based on their distinctive spectroscopic fingerprints that reflect, in particular, the extent of perturbation of vanadyl V=O bonds as a result of electrostatic interactions between the apical oxygen atoms and inserted Li-ions, as well as the strength of bonding between  $[VO_5]$  square pyramids along the  $V_2O_5$  sheets. <sup>22,47,48</sup> In Figure 4b, the vanadyl oxygen atoms are denoted as O1, and the in-plane connectivity between  $[VO_5]$  square pyramidal units through O2 and O3 atoms is also

illustrated. The observed Raman modes have been assigned based on normal mode analysis and prior phonon calculations by Baddour-Hadjean and co-workers; 22,47,48 complete spectral assignments can be found in the cited articles. Raman measurements suggest the predominance of the ε-Li<sub>x</sub>V<sub>2</sub>O<sub>5</sub> phase for the sample discharged to 3.26 V. Indeed, the prominent [VO<sub>5</sub>-VO<sub>5</sub>] mode is shifted from 145 cm<sup>-1</sup> for pristine V<sub>2</sub>O<sub>5</sub> nanowires to 150 cm<sup>-1</sup> for the discharged sample; furthermore, the vanadyl stretching mode is softened from 994 to 983 cm<sup>-1</sup>. The hardening of the former mode and its decreased relative intensity attest to the increased interaction between square pyramidal  $\mathrm{VO}_5$  units and the diminished longrange order upon lithiation of  $V_2O_5$ . The softening of the vanadyl Raman mode is furthermore consistent with a decrease in bond order of the vanadyl bonds in the  $\varepsilon$ -Li<sub>x</sub>V<sub>2</sub>O<sub>5</sub> phase as a result of electrostatic interactions between vanadyl oxygen atoms (O1) and the intercalated Li-ions. The Raman bands at 406, 525, and 699 cm<sup>-1</sup> for unlithiated V<sub>2</sub>O<sub>5</sub> are assigned to bond rocking oscillations involving apical O1 atoms, interchain stretching of V-O2 bonds, and antiphase stretching of V-O2 bonds, respectively. 22,47,48 These modes are shifted to 418, 534, and 704 cm<sup>-1</sup>, respectively, in the discharged sample (Figure 4a(ii)), reflective of the increased puckering of the layers in the  $\varepsilon$ -Li<sub>x</sub>V<sub>2</sub>O<sub>5</sub> phase. Upon discharge to still lower voltages, the 983 cm<sup>-1</sup> vanadyl Raman band is split into two distinct Raman bands: a 972 cm<sup>-1</sup> band ascribed to the incommensurately modulated  $\varepsilon'$ -Li<sub>x</sub>V<sub>2</sub>O<sub>5</sub> phase (x > 0.5) and a 989 cm<sup>-1</sup> band corresponding to  $\gamma$ -Li<sub>x</sub>V<sub>2</sub>O<sub>5</sub>. <sup>22</sup> A notable caveat is that Raman spectroscopy emphasizes surface contributions given its limited probe depth, and thus surface species make a disproportionately larger contribution to the measured signal.<sup>22</sup> Given that the nucleation and growth of  $\gamma$ -Li<sub>x</sub>V<sub>2</sub>O<sub>5</sub> from  $\varepsilon'$ -Li<sub>x</sub>V<sub>2</sub>O<sub>5</sub> likely commences at the surface of the nanowires upon supersaturation with Li-ions, lithiation gradients are likely from the Li-poor internal core to the Li-rich external surface, as has been observed in previous STXM measurements. 10 The  $\gamma$ -phase is observed by Raman spectroscopy even when it is present in relatively low amounts on Li-supersaturated surfaces of the nanowires. Upon further discharge down to 2.00 V, the disappearance of the broad Raman band at 972 cm<sup>-1</sup> as well as the appearance of a narrow band at 965 cm<sup>-1</sup> are indicative of the complete transformation to  $\gamma$ -Li<sub>x</sub>V<sub>2</sub>O<sub>5</sub> within the 50–100 nm probe depth of the Raman measurements.

In order to obtain a more quantitative measure of phase evolution across the entire volume fraction, powder XRD

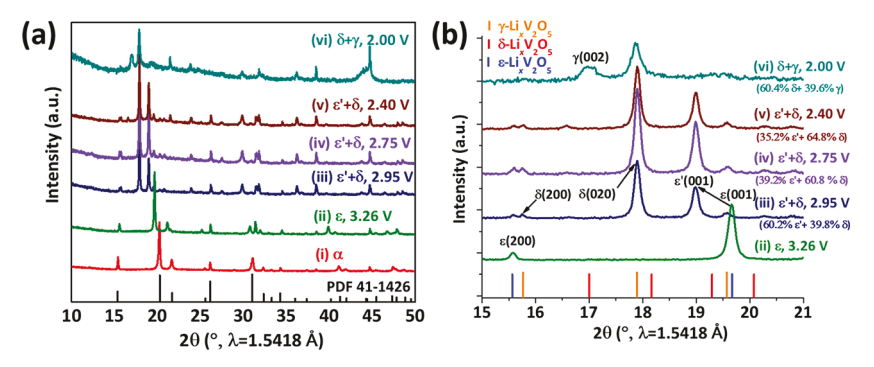


Figure 5. Powder XRD patterns of phase mixtures of discharged samples. (a) XRD patterns for (i) unlithiated V<sub>2</sub>O<sub>5</sub> contrasted to patterns acquired for electrochemically discharged V<sub>2</sub>O<sub>5</sub> samples collected at (ii) 3.26; (iii) 2.95; (iv) 2.75; (v) 2.40; and (vi) 2.00 V. (b) Magnified view of (a) with indexed reflections delineating various phases of Li<sub>x</sub>V<sub>2</sub>O<sub>5</sub>.

measurements have been acquired and the phase fractions have been determined based on Rietveld refinements as described in the Methods section. Figure 5 shows plots of the powder XRD patterns acquired for electrochemically lithiated V<sub>2</sub>O<sub>5</sub> at specific depths of discharge, whereas Table 1 enumerates the phase

Table 1. Phase Fractions Obtained from Rietveld Refinement of the XRD Patterns in Figure 5

	fractional coexistence of phases			
discharge voltage (V)	$\varepsilon$ -Li <sub>x</sub> V <sub>2</sub> O <sub>5</sub>	$\varepsilon'$ -Li <sub>x</sub> V <sub>2</sub> O <sub>5</sub>	$\delta$ -Li <sub>x</sub> V <sub>2</sub> O <sub>5</sub>	$\gamma$ -Li <sub>x</sub> V <sub>2</sub> O <sub>5</sub>
3.26	1.00	0	0	0
2.95	0	0.602	0.398	0
2.75	0	0.392	0.608	0
2.40	0	0.352	0.648	0
2.00	0	0	0.604	0.396

fractions, furnishing a detailed perspective of the underlying intercalation-induced structural transformations.<sup>22</sup> Refinement fit statistics and lattice parameters are noted in Table S1 (Supporting Information). The unlithiated V<sub>2</sub>O<sub>5</sub> powder [labeled as (i) in Figure 5] can be indexed to the orthorhombic shcherbinaite phase of V<sub>2</sub>O<sub>5</sub> [Joint Committee on Powder Diffraction Standards (JCPDS) #41-1426]. Upon discharge to 3.26 V, the (001) interlayer separation is increased from 4.39 to 4.52 Å, reflective of the stabilization of the  $\varepsilon$ -Li<sub>x</sub>V<sub>2</sub>O<sub>5</sub> phase with an expanded interlayer separation. The XRD patterns for the discharged samples at 2.95, 2.75, and 2.40 V indicate the coexistence of both the incommensurately modulated  $\varepsilon'$ - and higher-Li-content  $\delta$ -phases of  $\text{Li}_x \text{V}_2 \text{O}_5$ . The appearance of a reflection at  $2\theta = 19.00^{\circ}$ , indexed to the 4.67 Å (001) interlayer separation of the  $\varepsilon'$ -phase, suggests stabilization of the incommensurately modulated  $\varepsilon'$  structure. In this structure, stabilized for x > 0.53 in  $\text{Li}_x \text{V}_2 \text{O}_5$ , Li-ions can no longer simply occupy alternate cubooctahedral sites, and as a result, need to be situated in adjacent sites.<sup>49</sup> The reflections corresponding to lattice spacings of d = 5.63 and 4.94 Å at  $2\theta = 15.75^{\circ}$  and  $17.95^{\circ}$ can be indexed to (200) and (020) planes of the  $\delta$ -phase,

The  $\gamma$ -phase is discernible in the sample discharged to 2.00 V based on the appearance of its characteristic (002) reflection at  $2\theta = 17.00^{\circ}$ . Figure 5b shows a magnified view of the XRD patterns with the indexed characteristic reflections delineating the different phases of Li<sub>x</sub>V<sub>2</sub>O<sub>5</sub>. Table 1 presents the fractional proportions of each of the phases recovered at different discharge voltages as determined from Rietveld refinements following the procedures noted in the Methods section. At 3.26

V, the pattern can be indexed solely to  $\varepsilon$ -Li<sub>x</sub>V<sub>2</sub>O<sub>5</sub> within the limits of detection, as also corroborated by the Raman measurements in Figure 4. Indeed, this observation is consistent with the sharp decrease in voltage within the 3.34-3.25 V window wherein lithiation proceeds through a monophasic regime assigned as shown in Figure 2. Indeed, the Li-ion diffusivity is on the order of  $10^{-10}$  cm<sup>2</sup>·s<sup>-1</sup> for this sample, which is at the higher end of the Li-ion diffusivity range measured in this study. At 2.95 V, the sample is a mixture of  $\varepsilon'$ -Li<sub>x</sub>V<sub>2</sub>O<sub>5</sub> and  $\delta$ -Li<sub>x</sub>V<sub>2</sub>O<sub>5</sub> (in an approximately 3:2 ratio). At still lower discharge voltages, the proportion of the  $\delta$ -phase is increased, approaching 65% of the sample at 2.40 V (Table 1). The observed nucleation and growth of the  $\delta$ -phase at the expense of the  $\varepsilon'$ -phase with an extended phase coexistence regime is characteristic of phasetransforming electrodes, and is indeed analogous to nucleation and growth of Li-rich phases observed by principal component analysis of V K-edge X-ray absorption near-edge structure (XANES) spectroscopy for chemically lithiated V<sub>2</sub>O<sub>5</sub>. Notably, the mixture of phases coincides with a pronounced dip of Li-ion diffusivity (down to  $4 \times 10^{-13}$  cm<sup>2</sup>·s<sup>-1</sup> at 2.40 V) in Figure 3. At a discharge voltage of 2.00 V, the highly lithiated  $\gamma$ phase begins to emerge at the expense of the  $\delta$ -phase, as also corroborated by Raman spectroscopy in Figure 4. The phase coexistence regime is again marked by a pronounced dip of Liion diffusivity down to  $10^{-14}$  cm<sup>2</sup>·s<sup>-1</sup>, among the lowest values measured in this study (Figure 3).

On the basis of evaluation of Figures 3-5 and Table 1, sharp dips of Li-ion diffusivity appear to coincide with phase coexistence regimes, whereas the diffusivity is high in voltage windows where a single phase is dominant. No substantial diminution of  $D_{1i}$  is observed across the  $\alpha \to \varepsilon$  transformation, likely as a result of close structural homology between the two phases. At ca. 3.26 V, the monophasic  $\varepsilon$ -phase, as indicated by powder XRD (Figure 5) and Raman spectroscopy (Figure 4a), shows a high Li-ion diffusivity of  $8 \times 10^{-11}$  cm<sup>2</sup>·s<sup>-1</sup>. However, a pronounced reduction of diffusivity is observed at 2.60 V, correlated with the nucleation of  $\delta$ -Li<sub>x</sub>V<sub>2</sub>O<sub>5</sub> and coexistence of the  $\varepsilon'$ - and  $\delta$ -phases. Similar reductions of diffusivity are observed to be correlated with  $\delta - \gamma$  and  $\gamma - \omega$  phase coexistence regimes. These findings are suggestive that the reduction in diffusivity of ions is related to phase boundaries formed between phases during nucleation and growth processes in multiphasic

In order to verify the aforementioned hypothesis that phase boundaries and not intrinsic differences in Li-ion diffusivity underpin the observed four-orders-of-magnitude changes of  $D_{Li}$ , as suggested by structural characterization of the discharged

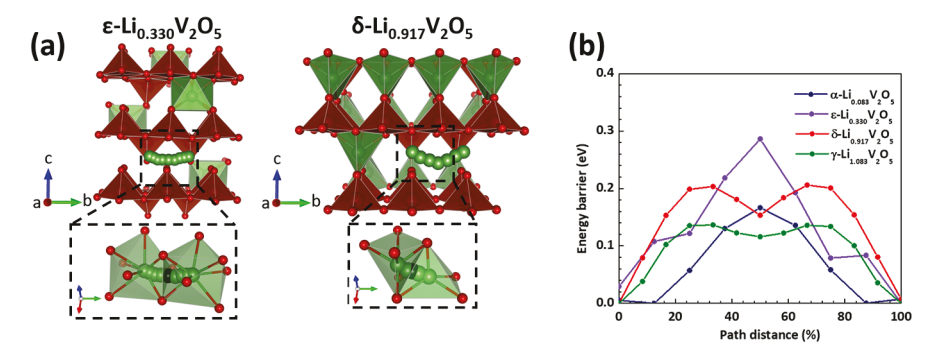


Figure 6. Diffusion pathways and Li-ion migration barriers in  $\text{Li}_x \text{V}_2 \text{O}_5$ . (a) Diffusion pathways and alterations of the Li-ion coordination environment during Li-ion diffusion through ε-Li<sub>0.33</sub>V<sub>2</sub>O<sub>5</sub> and δ-Li<sub>0.917</sub>V<sub>2</sub>O<sub>5</sub>. [VO<sub>5</sub>] units are represented as red polyhedra and [LiO<sub>x</sub>] units are shown as green polyhedra; the green and red spheres represent lithium and oxygen atoms, respectively; the transition states are denoted by a darker shading. (b) Diffusion energy barrier calculated for Li-ions in α- Li<sub>0.083</sub>V<sub>2</sub>O<sub>5</sub>, ε-Li<sub>0.330</sub>V<sub>2</sub>O<sub>5</sub>, δ-Li<sub>0.917</sub>V<sub>2</sub>O<sub>5</sub>, and γ-Li<sub>1.083</sub>V<sub>2</sub>O<sub>5</sub>.

Table 2. Changes in Local Li-Ion Coordination Environment, Calculated Migration Barriers Encountered by Li-Ion, and Extrapolated Diffusivities of Li-Ion in Lithiated Phases of  $V_2O_5$ 

lithiated phase of $V_2O_5$	change in the coordination environment of Li-ion	Li-ion migration barrier (eV)	diffusivity of Li-ion $(cm^2 \cdot s^{-1})$	refs
$\alpha$ -Li <sub>0.083</sub> V <sub>2</sub> O <sub>5</sub>	$8 \rightarrow 3 \rightarrow 8$	0.17	$5.99 \times 10^{-8}$	50
$\varepsilon$ -Li <sub>0.330</sub> V <sub>2</sub> O <sub>5</sub>	$8 \rightarrow 3 \rightarrow 8$	0.29	$5.30 \times 10^{-8}$	this work
$\delta$ -Li <sub>0.917</sub> V <sub>2</sub> O <sub>5</sub>	$5 \to 3 \to 6 \to 3 \to 5$	0.20	$5.97 \times 10^{-8}$	this work
$\gamma$ -Li <sub>1.083</sub> V <sub>2</sub> O <sub>5</sub>	$5 \to 3 \to 4 \to 3 \to 5$	0.13	$6.47 \times 10^{-8}$	51

samples and the GITT measurements, first-principles DFT calculations have been used to evaluate the migration barriers in each of the lithiated phases of Li<sub>x</sub>V<sub>2</sub>O<sub>5</sub> In previous work, NEB calculations have been used to evaluate ion migration and polaron diffusion barriers in orthorhombic V2O5 as well as several metastable polymorphs of  $V_2O_5$ . So  $^{50-54}$  These studies have established that the diffusion barriers depend sensitively on the local coordination environments that can be accessed by Li-ions, which in turn depend sensitively on the stacking sequence and extent of puckering of  $V_2O_5$  layers.<sup>42,50–52,54,55</sup> Figure 6a illustrates the diffusion pathways followed by Li-ions in  $\varepsilon$ - and  $\delta$ lithiated phases. The lowest energy diffusion pathways involve a change of the Li-ion coordination environment from  $8 \rightarrow 3 \rightarrow 8$ in  $\varepsilon$ -Li<sub>0.330</sub>V<sub>2</sub>O<sub>5</sub> and 5  $\rightarrow$  3  $\rightarrow$  6  $\rightarrow$  3  $\rightarrow$  5 in  $\delta$ -Li<sub>0.917</sub>V<sub>2</sub>O<sub>5</sub>. Diffusion pathways for Li-ions in  $\alpha$ - and  $\gamma'$ -V<sub>2</sub>O<sub>5</sub>, deduced from analogous NEB calculations, have been published elsewhere. 50,51 Figure 6b shows plots of the energies along the diffusion pathway as determined from NEB calculations, thereby providing a measure of the migration barriers. Table 2 enumerates the changes in local coordination environment, calculated migration barriers, and extrapolated diffusivities for Li-ions in each of the lithiated phases (the  $\omega$ -phase is highly disordered and a clear structure elucidation has remained elusive for this structure). 4 α-Li<sub>0.083</sub>V<sub>2</sub>O<sub>5</sub> displays an activation barrier of 0.17 eV per unit cell with Li-ions forced to traverse a trigonal planar site in diffusing between cubooctahedral environments.<sup>5</sup> Upon transformation to the distorted  $\varepsilon$ -phase, the trigonal site where ions reside is further constricted and as a result of increased cation-cation repulsions, the migration barrier is increased by 0.12 eV. Interestingly, upon transformation to the  $\delta$ -phase, Li-ions in  $\delta$ -Li<sub>0.917</sub>V<sub>2</sub>O<sub>5</sub> encounter a migration barrier of 0.20 eV with an entirely distinctive diffusion pathway involving two transition states (Figure 6a).<sup>4,50,51</sup> The  $\gamma$ -Li<sub>1.083</sub>V<sub>2</sub>O<sub>5</sub> phase shows the lowest migration barrier of 0.13 eV for the diffusion of Li-ions; this reduction of the energy barrier can be ascribed to a relatively spacious square-planar transition-state intermediate between the tetrahedral Li-ion sites.<sup>51</sup> A first approximation of

diffusivities (D) can be obtained from the calculated activation energy barriers as per

$$D = d^2 \nu^* \exp(-E_{act}/k_{\rm B}T) \tag{3}$$

where  $E_{act}$  is the calculated migration barrier (Table 2),  $k_{\rm B}$  is the Boltzmann constant, T is the temperature,  $v^*$  is the attempt frequency, and d is the hopping distance. Diffusivity values extrapolated from the calculated barriers at room temperature using eq 3 for a hopping distance of 4.0 Å assuming an attempt frequency  $v^*$  of 3 × 10<sup>13</sup> Hz are enumerated in Table 2.<sup>50,51</sup> These diffusivity values are not surprisingly substantially different from the ca.  $5.50 \times 10^{-11}$  to  $2 \times 10^{-14}$  cm<sup>2</sup>·s<sup>-1</sup> experimental diffusivity values noted above and reported in the literature because the calculations account only for atomistic diffusion barriers and not interfacial diffusion barriers encountered at particle interfaces and across extended defects. 10,50,57,58 It is instructive that the extrapolated values deduced from the calculated activation energy barriers are within ca. 25% of each other and are thus not explicative of the large experimental modulations of diffusivity measured across the sequence of intercalation-induced transformations. Consequently, the 4 orders of magnitude variation of Li-ion diffusivity observed in GITT experiments derives from the stabilization and elimination of phase boundaries and does not reflect intrinsic differences in the ionic conductivity of the different lithiated phases.

In order to distinguish between individual particles, each of a different phase and phase boundaries within individual particles, STXM measurements have been utilized across the V L- and O K-edges to evaluate the formation of phase boundaries and lithiation gradients within individual particles. Measuring XANES features at these edges, corresponding to transitions of core electrons to unoccupied and partially occupied states, provides a means of examining electron localization accompanying electrochemical discharge. Figure 7a depicts an STXM image acquired for a discharged sample recovered at 2.95 V, corresponding to a mixture of  $\varepsilon'$  and  $\delta$  phases as per Figure 5

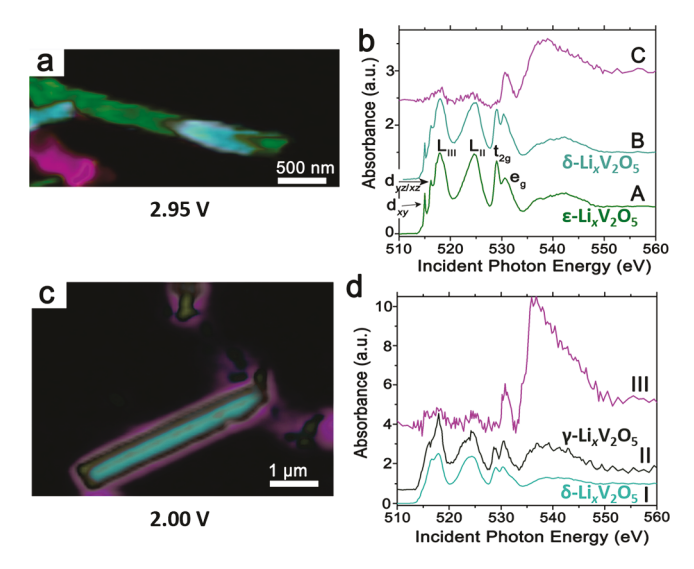


**Figure 7.** STXM imaging of lithiation gradients and phase boundaries: SVD STXM maps and component spectra for Li<sub>x</sub>V<sub>2</sub>O<sub>5</sub> particles recovered at discharge states of (a,b) 2.95 and (c,d) 2.00 V. The stabilization of phase boundaries between green and cyan (b) or cyan and gray (d) domains is clearly discernible for both samples. (b) Spectra A, B, and C represent spectral components corresponding to domains depicted in the same color in panel (a). Spectrum A corresponds to a lower extent of lithiation as compared to spectrum B given the higher intensity of the V  $3d_{xy}$  and  $3d_{xz/yz}$  features at the V L<sub>III</sub>-edge and the higher ratio of  $t_{2g}/e_g^*$  absorption features at the O K-edge. Spectrum C corresponds to surficial lithium oxide species. (d) Spectra I, II, and III represent spectral components corresponding to domains depicted in the same color in panel (c). Spectrum I corresponds to a relatively less lithiated domain as compared to spectrum II based on the relative ratio of the  $t_{2g}$  and  $e_g^*$  absorption features. Spectrum III corresponds to surficial lithium oxide species.

and Table 1, alongside the component spectra derived from SVD analysis of the entire hyperspectral data set. Figure 7c shows an STXM image acquired for a discharged sample recovered at 2.00 V, corresponding to a mixture of the  $\delta$ - and  $\gamma$ phases of Li<sub>x</sub>V<sub>2</sub>O<sub>5</sub>, again with the component spectra plotted alongside. Figure S2 (Supporting Information) contrasts V Land O K-edge integrated spectra obtained for these two samples with a spectrum acquired for unlithiated V<sub>2</sub>O<sub>5</sub>. Figure 7a,c maps the spatial distribution of the distinct spectral components attributed to different lithiated domains within samples at discharge states of 2.95 and 2.00 V, respectively; the spectral components from ROI deconvolution are plotted in Figure 7b,d. In other words, the images in Figure 7a,c represent the pixel-wise spatial localization of the spectral components such that each pixel is shaded with the color of the component that has the majority contribution within that region.

The lineshapes and relative intensities of V L- and O K-edge X-ray absorption spectra contain a wealth of information regarding the formal oxidation state and depth of discharge of the  $V_2O_5$  particles upon lithiation. The V L-edge features labeled as such in Figures 7b and S2 correspond to transitions from V  $2p_{3/2} \rightarrow V$  3d (ca. 518 eV, designated as V L<sub>II</sub>) and V  $2p_{1/2} \rightarrow V$  3d (ca. 525 eV, designated as V L<sub>II</sub>) states, respectively, which is consistent with the dipole-selection rules governing core-level electronic spectroscopy, wherein allowed transitions correspond to a change in the angular momentum quantum number,  $\Delta l = \pm 1$ . The separation of ca. 7 eV between these features is reflective of the spin—orbit coupling characteristic of a pentavalent oxidation state for vanadium.

The operation of a Coster-Krönig Auger emission process and the resulting line-broadening renders the V L<sub>II</sub> edge less informative; however, in contrast, the V L<sub>III</sub> spectral feature provides an excellent perspective of the bottom edge of the conduction band of Li<sub>x</sub>V<sub>2</sub>O<sub>5</sub>. These resonances correspond to transitions from a singlet V 2p<sup>6</sup>3d<sup>0</sup> electronic configuration to a V 2p<sup>5</sup>3d<sup>1</sup> state, which yields a rich manifold of sub-levels as a result of crystal field splitting and multiplet effects. 60 The first two sharp features at 515.6 and 516.8 eV can be assigned to final states that are predominantly  $3d_{xy}$  and  $3d_{xz/yz}$  in character, respectively. 61,63 The insertion of Li-ions brings about a formal reduction of the vanadium center. As a result of the increased electron occupancy of the lowest lying V  $3d_{xy}$  and  $3d_{xz/yz}$  states upon electrochemical discharge and insertion of Li-ions, <sup>21</sup> the intensity of these features is attenuated as a result of Pauli blocking as can be clearly seen in Figure S2, contrasting integrated spectra for the discharged samples with that of unlithiated V<sub>2</sub>O<sub>5</sub>. <sup>21,42</sup> Consequently, the diminished intensity of low-energy V L<sub>III</sub> features serves as an excellent proxy for the extent of lithiation of V<sub>2</sub>O<sub>5</sub>.<sup>64</sup>

Spectral features at the O K-edge probe transition from O 1s to O 2p states; the considerable hybridization of the latter with V 3d states results in two distinct sets of resonances (with approximately t<sub>2g</sub> and e<sub>g</sub> symmetry reflective of the quasioctahedral coordination of vanadium atoms; as delineated in Figures 7b and S2) and makes the spectra an excellent probe of crystal field splitting of the transition-metal 3d states. On the basis of excited-state core-hole calculations, the  $t_{2g}$ absorption feature (ca. 529 eV) is derived primarily from the hybridization of vanadyl oxygen states with V  $3d_{xz/yz}$  states as well as from the mixing of the  $2p_y$  orbital and the  $2p_x$  orbital with V 3d<sub>xy</sub> states.<sup>21</sup> In turn, the e<sub>g</sub> absorption (centered at ca. 531 eV) corresponds to transitions to O 2p states hybridized with V  $3d_{z^{2}}$  and  $\sqrt{3}d_{x^{2}-y^{2}}$  states that are relatively raised in energy as a result of end-on metal-ligand  $\sigma$  interactions. Consistent with previous work in this system, Li-ion intercalation strongly modifies the O K-edge XANES spectrum. 10,15,21 In particular, the relative ratio between the  $t_{2g}$  and  $e_g^{\ast}$  intensities is greatly modified as a result of the lifting of the electron spin degeneracy and the emergence of electron correlation (as the system goes from a V5+ 3d0 system to a mixed-valence system with a considerable abundance of V<sup>4+</sup> 3d<sup>1</sup> sites) accompanied by a distortion of the structural lattice, which raises the energy of the  $\pi$ -bonded t<sub>2g</sub> states. <sup>21,42</sup> Figure S2 contrasts integrated spectra acquired for samples discharged to 2.95 and 2.00 V with the spectrum of unlithiated V<sub>2</sub>O<sub>5</sub>, illustrating that the relative intensity of the low-energy V  $L_{\text{III}}$ -edge features and the relative ratio of the  $t_{2g}$  and  $e_g$  absorptions at the O K-edge serve as excellent measures of the Li-ion concentration within these particles.

Considering the two spectral components plotted in Figure 7b for the sample recovered at 2.95 V, the green spectrum (labeled A) corresponds to a lower extent of lithiation as compared to spectrum B given the higher intensity of the V  $3d_{xy}$  and  $3d_{xz/yz}$  features at the V  $L_{III}$ -edge and the higher ratio of  $t_{2g}/e_g^*$  absorption features at the O K-edge. Figure 7a depicts a false color map, plotting the spatial distribution of the color-coded spectral components. The green domain of the image corresponds to a relatively less lithiated region, whereas the cyan-shaded region reflects a greater weighting of the higher Licontent spectrum B. A clear phase boundary is discernible between the cyan and green domains. The formation of such phase boundaries can be correlated with reduced Li-ion

diffusivity. The magenta area corresponds primarily to amorphous lithium oxide species formed from brief exposure to air as noted in past studies of electrochemically discharged compounds.65

For the sample discharged to 2.00 V, the spectral components extracted from SVD analysis (Figure 7d) of the integrated spectrum in Figure S2 suggest a greater extent of lithiation, evidenced by the almost complete attenuation of the V 3d<sub>xy</sub> and  $3d_{xz/yz}$  absorption features and the higher intensity of the  $e_g^*$ resonance as compared to the t2g resonance. The spectral component denoted as I in Figure 7d corresponds to a relatively less lithiated domain as compared to Spectrum II based on the relative ratio of the  $t_{2g}$  and  $e_g^*$  absorption features. The STXM map in Figure 7c indicates a strip of the higher lithiated gray domain (corresponding to the gray spectrum II component), reflecting a core-shell gradient of the Li-ion concentration. The magenta regions are again assigned to primarily LixOv contributions as seen before with electrochemically discharged Ag<sub>2</sub>VO<sub>2</sub>PO<sub>4</sub> samples.<sup>65</sup> The observation of several domains separated by phase boundaries within individual nanowires is correlated to a clear diminution in diffusivity values. Figure 8

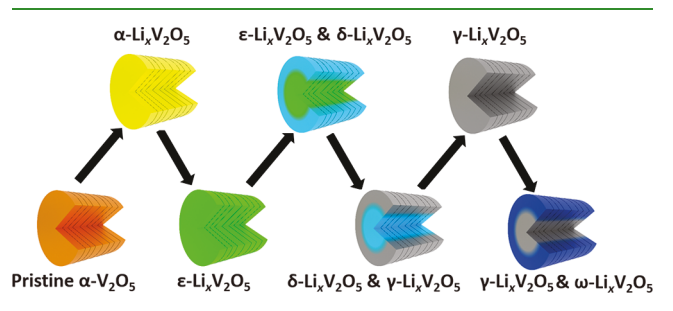


Figure 8. Schematic illustration of phase progression with increasing Liion intercalation (greater depth of discharge). The graphic depicts phase coexistence regimes and phase boundaries that bring about sharp dips of Li-ion diffusivities.

illustrates the progression of phase nucleation and growth upon Li-ion insertion, resulting in stabilization of phase boundaries that serve as an impediment to Li-ion diffusion. On the basis of GITT measurements, phase boundaries can bring about up to a 10<sup>4</sup> diminution of Li-ion diffusivity.

## 4. CONCLUSIONS

The coupled diffusion of electrons and ions within electrode materials and across interfaces underpins the power density that can be viably extracted from a battery and determines its rate capabilities. Insertion of Li-ions profoundly alters the local structure of cathode materials, in some cases, bringing about energy-dissipative phase transformations. Such phase transformations require the creation and motion of dislocations at the interface between the parent lattice and the nucleated Li-rich phase. Using  $\alpha$ -V<sub>2</sub>O<sub>5</sub> as a cathode material given its multiple intercalation-induced transformations, we evidence using GITT measurements, the transport penalties incurred as a result of the formation of such interfaces. Sharp dips in Li-ion diffusion coefficients are observed to be correlated with phase coexistence regimes characterized by phase boundaries within particles. A 10<sup>4</sup> decrease of Li-ion diffusivity can be attributed to the increased transport resistance resulting from the creation of phase boundaries. In contrast, monophasic regimes are characterized by the highest values of Li-ion diffusion coefficients within the measured range. NEB DFT calculations

have been used to establish that such variances are not derived from intrinsic differences in migration barriers across the different lithiated phases. In addition to structural characterization by ensemble Raman spectroscopy and powder XRD measurements correlating sharps dips of Li-ion diffusivity to phase mixtures, clear lithiation gradients and phase boundaries are evidenced within individual actively intercalating particles using STXM mapping across the V  $L_{\text{III}}$ - and O K-edges. The results therefore provide a remarkable demonstration of how interfacial phenomena, mapped using spectroscopic signatures of the electronic structure, can alter macroscopic electrode properties. The results suggest that an important imperative for such materials to be used within high-rate batteries will be to use precise nanoscale texturation to suppress stabilization of phase boundaries and promote Li-ion uptake by solid-solution formation, which is thought to occur in V2O5 below a critical size of 40-50 nm. 4,23 Delineation of precise resistivity contributions of individual phase boundaries is thus far inaccessible from experiment or first-principles calculations. Modeling of large supercells incorporating transformation dislocations is necessary to examine the modulation of Li-ion diffusivity across such extended defects but has not thus far been achieved, given the considerable computational expense. In previous work, several of the authors have modeled the phase boundary resistance of Si- and Sn-based alloying anode materials. 66,67 In these materials, volume expansion is a major contributor; however, mesoscale models examining the implications of phase boundaries in low-volume expansion cathode materials such as V<sub>2</sub>O<sub>5</sub> have not thus far been developed and will be the focus of future efforts, given the clear delineation of the macroscopic influence of phase interfaces determined here and the nanoscopic identification of phase boundaries enabled here by STXM (core-shell and striping motifs have been identified).

## **ASSOCIATED CONTENT**

## S Supporting Information

The Supporting Information is available free of charge on the ACS Publications website at DOI: 10.1021/acsami.8b10604.

Powder XRD patterns of samples discharged at different voltages; Rietveld refinement statistics and lattice parameters for each of the powder XRD patterns; and V L<sub>III</sub> and O K-edge integrated spectra obtained for samples discharged 2.95 and 2.00 V contrasted with the spectrum of unlithiated V<sub>2</sub>O<sub>5</sub> (PDF)

#### AUTHOR INFORMATION

## **Corresponding Authors**

\*E-mail: pmukherjee@purdue.edu (P.P.M.).

\*E-mail: banerjee@chem.tamu.edu (S.B.).

ORCID ©

Sarbajit Banerjee: 0000-0002-2028-4675

The authors declare no competing financial interest.

# **ACKNOWLEDGMENTS**

This study is based on work supported by the National Science Foundation (NSF) under DMR 1809866. L.R.D.J. acknowledges support under a NSF Graduate Research Fellowship under grant no. 1252521. A portion of the research described in this review was performed at the Canadian Light Source, which is supported by the Natural Sciences and Engineering Research Council of Canada, the National Research Council Canada, the Canadian Institutes of Health Research, the Province of Saskatchewan, Western Economic Diversification Canada, and the University of Saskatchewan. J.L.A. acknowledges support from a NASA Fellowship under 80NSSC17K0182. A.P. acknowledges support from the Advanced Light Source (ALS) doctoral fellowship in residence. A portion of the calculations were executed at the Molecular Foundry, Lawrence Berkeley National Laboratory, which is supported by the Office of Science, Office of Basic Energy Sciences, of the U.S. Department of Energy, under contract number DE-AC02-05CH11231. D.J.R. acknowledges support from the NSF under grant no. 1759651. P.P.M. acknowledges support from NSF under grant no. 1438431.

#### REFERENCES

- (1) Goodenough, J. B. Rechargeable Batteries: Challenges Old and New. J. Solid State Electrochem. 2012, 16, 2019–2029.
- (2) Tarascon, J.-M.; Armand, M. Issues and Challenges Facing Rechargeable Lithium Batteries. *Nature* **2001**, 414, 359–367.
- (3) Etacheri, V.; Marom, R.; Elazari, R.; Salitra, G.; Aurbach, D. Challenges in the Development of Advanced Li-Ion Batteries: A Review. *Energy Environ. Sci.* **2011**, *4*, 3243–3262.
- (4) De Jesus, L. R.; Andrews, J. L.; Parija, A.; Banerjee, S. Defining Diffusion Pathways in Intercalation Cathode Materials: Some Lessons from  $V_2O_5$  on Directing Cation Traffic. ACS Energy Lett. **2018**, 3, 915–931
- (5) Meng, Y. S.; Arroyo-de Dompablo, M. E. Recent Advances in First Principles Computational Research of Cathode Materials for Lithium-Ion Batteries. *Acc. Chem. Res.* **2013**, *46*, 1171–1180.
- (6) Van der Ven, A.; Bhattacharya, J.; Belak, A. A. Understanding Li Diffusion in Li-Intercalation Compounds. *Acc. Chem. Res.* **2013**, *46*, 1216–1225.
- (7) Weker, J. N.; Liu, N.; Misra, S.; Andrews, J. C.; Cui, Y.; Toney, M. F. Insitu nanotomography and operando transmission X-ray microscopy of micron-sized Ge particles. *Energy Environ. Sci.* **2014**, *7*, 2771–2777.
- (8) Chen, C.-F.; Barai, P.; Mukherjee, P. P. Diffusion Induced Damage and Impedance Response in Lithium-Ion Battery Electrodes. *J. Electrochem. Soc.* **2014**, *161*, A2138–A2152.
- (9) Persson, K.; Sethuraman, V. A.; Hardwick, L. J.; Hinuma, Y.; Meng, Y. S.; van der Ven, A.; Srinivasan, V.; Kostecki, R.; Ceder, G. Lithium Diffusion in Graphitic Carbon. *J. Phys. Chem. Lett.* **2010**, *1*, 1176–1180.
- (10) De Jesus, L. R.; Zhao, Y.; Horrocks, G. A.; Andrews, J. L.; Stein, P.; Xu, B.-X.; Banerjee, S. Lithiation across interconnected  $\rm V_2O_5$  nanoparticle networks. *J. Mater. Chem. A* **2017**, *5*, 20141–20152.
- (11) Abdellahi, A.; Akyildiz, O.; Malik, R.; Thornton, K.; Ceder, G. Particle-size and morphology dependence of the preferred interface orientation in LiFePO<sub>4</sub> nano-particles. *J. Mater. Chem. A* **2014**, 2, 15437–15447.
- (12) Wang, J.; Yang, J.; Tang, Y.; Liu, J.; Zhang, Y.; Liang, G.; Gauthier, M.; Karen Chen-Wiegart, Y.-C.; Norouzi Banis, M.; Li, X.; Li, R.; Wang, J.; Sham, T. K.; Sun, X. Size-Dependent Surface Phase Change of Lithium Iron Phosphate during Carbon Coating. *Nat. Commun.* **2014**, *5*, 3415.
- (13) Yu, Y.-S.; Kim, C.; Shapiro, D. A.; Farmand, M.; Qian, D.; Tyliszczak, T.; Kilcoyne, A. L. D.; Celestre, R.; Marchesini, S.; Joseph, J.; Denes, P.; Warwick, T.; Strobridge, F. C.; Grey, C. P.; Padmore, H.; Meng, Y. S.; Kostecki, R.; Cabana, J. Dependence on Crystal Size of the Nanoscale Chemical Phase Distribution and Fracture in Li<sub>x</sub>FePO<sub>4</sub>. *Nano Lett.* **2015**, *15*, 4282–4288.
- (14) Lim, J.; Li, Y.; Alsem, D. H.; So, H.; Lee, S. C.; Bai, P.; Cogswell, D. A.; Liu, X.; Jin, N.; Yu, Y.-s.; Salmon, N. J.; Shapiro, D. A.; Bazant, M. Z.; Tyliszczak, T.; Chueh, W. C. Origin and Hysteresis of Lithium

- Compositional Spatiodynamics within Battery Primary Particles. *Science* **2016**, 353, 566–571.
- (15) De Jesus, L. R.; Stein, P.; Andrews, J. L.; Luo, Y.; Xu, B.-X.; Banerjee, S. Striping Modulations and Strain Gradients within Individual Particles of a Cathode Material upon Lithiation. *Mater. Horizon.* **2018**, *5*, 486–498.
- (16) Yu, Y. S.; Farmand, M.; Kim, C.; Liu, Y.; Grey, C. P.; Strobridge, F. C.; Tyliszczak, T.; Celestre, R.; Denes, P.; Joseph, J.; Krishnan, H.; Maia, F. R. N. C.; Kilcoyne, A. L. D.; Marchesini, S.; Leite, T. P. C.; Warwick, T.; Padmore, H.; Cabana, J.; Shapiro, D. A. Three-Dimensional Localization of Nanoscale Battery Reactions Using Soft X-Ray Tomography. *Nat. Commun.* **2018**, *9*, 921.
- (17) Enjalbert, R.; Galy, J. A refinement of the structure of V<sub>2</sub>O<sub>5</sub>. Acta Crystallogr., Sect. C: Cryst. Struct. Commun. **1986**, 42, 1467–1469.
- (18) Galy, J. Vanadium pentoxide and vanadium oxide bronzes-Structural chemistry of single (S) and double (D) layer  $M_xV_2O_5$  phases. J. Solid State Chem. **1992**, 100, 229–245.
- (19) Artuso, F.; Decker, F.; Krasilnikova, A.; Liberatore, M.; Lourenco, A.; Masetti, E.; Pennisi, A.; Simone, F. Indium—Vanadium Oxides Deposited by Radio Frequency Sputtering: New Thin Film Transparent Materials for Li-Insertion Electrochemical Devices. *Chem. Mater.* 2002, 14, 636–642.
- (20) Mège, S.; Levieux, Y.; Ansart, F.; Savariault, J. M.; Rousset, A. Electrochemical Properties of a New V<sub>2</sub>O<sub>5</sub> Xerogel. *J. Appl. Electrochem.* **2000**, 30, 657–664.
- (21) De Jesus, L. R.; Horrocks, G. A.; Liang, Y.; Parija, A.; Jaye, C.; Wangoh, L.; Wang, J.; Fischer, D. A.; Piper, L. F. J.; Prendergast, D.; Banerjee, S. Mapping polaronic states and lithiation gradients in individual  $V_2O_5$  nanowires. *Nat. Commun.* **2016**, *7*, 12022.
- (22) Horrocks, G. A.; Likely, M. F.; Velazquez, J. M.; Banerjee, S. Finite size effects on the structural progression induced by lithiation of  $V_2O_5$ : a combined diffraction and Raman spectroscopy study. *J. Mater. Chem. A* **2013**, *1*, 15265–15277.
- (23) Zhao, Y.; De Jesus, L. R.; Stein, P.; Horrocks, G. A.; Banerjee, S.; Xu, B.-X. Modeling of Phase Separation across Interconnected Electrode Particles in Lithium-Ion Batteries. *RSC Adv.* **2017**, 7, 41254–41264.
- (24) Weppner, W.; Huggins, R. A. Determination of the Kinetic Parameters of Mixed-Conducting Electrodes and Application to the System Li<sub>3</sub>Sb. *J. Electrochem. Soc.* **1977**, *124*, 1569–1578.
- (25) Yang, S.; Wang, X.; Yang, X.; Bai, Y.; Liu, Z.; Shu, H.; Wei, Q. Determination of the chemical diffusion coefficient of lithium ions in spherical Li[Ni<sub>0.5</sub>Mn<sub>0.3</sub>Co<sub>0.2</sub>]O<sub>2</sub>. *Electrochim. Acta* **2012**, *66*, 88–93.
- (26) Verma, A.; Smith, K.; Santhanagopalan, S.; Abraham, D.; Yao, K. P.; Mukherjee, P. P. Galvanostatic Intermittent Titration and Performance Based Analysis of LiNi<sub>0.5</sub>Co<sub>0.2</sub>Mn<sub>0.3</sub>O<sub>2</sub> Cathode. *J. Electrochem. Soc.* **2017**, *164*, A3380–A3392.
- (27) Zhu, Y.; Wang, C. Galvanostatic Intermittent Titration Technique for Phase-Transformation Electrodes. *J. Phys. Chem. C* **2010**, *114*, 2830–2841.
- (28) Dees, D. W.; Abraham, D. P.; Lu, W.; Gallagher, K. G.; Bettge, M.; Jansen, A. N. Electrochemical Modeling and Performance of a Lithium- and Manganese-Rich Layered Transition-Metal Oxide Positive Electrode. *J. Electrochem. Soc.* **2015**, *162*, A559–A572.
- (29) Dees, D. W.; Kawauchi, S.; Abraham, D. P.; Prakash, J. Analysis of the Galvanostatic Intermittent Titration Technique (GITT) as Applied to a Lithium-Ion Porous Electrode. *J. Power Sources* **2009**, *189*, 263–268
- (30) Rajagopal, A. K.; Callaway, J. Inhomogeneous Electron Gas. *Phys. Rev. B: Solid State* **1973**, *7*, 1912–1919.
- (31) Kohn, W.; Sham, L. J. Self-Consistent Equations Including Exchange and Correlation Effects. *Phys. Rev.* **1965**, *140*, A1133–A1138.
- (32) Perdew, J. P.; Burke, K.; Ernzerhof, M. Generalized Gradient Approximation Made Simple. *Phys. Rev. Lett.* **1996**, *77*, 3865–3868.
- (33) Toby, B. H. EXPGUI, a graphical user interface for GSAS. *J. Appl. Crystallogr.* **2001**, *34*, 210–213.
- (34) Cava, R. J.; Santoro, A.; Murphy, D. W.; Zahurak, S. M.; Fleming, R. M.; Marsh, P.; Roth, R. S. The structure of the lithium-inserted metal oxide  $\delta$ -LiV<sub>2</sub>O<sub>5</sub>. *J. Solid State Chem.* **1986**, *65*, *63*–71.

- (35) Anderson, D. N.; Willett, R. D. Refinement of the structure of LiV<sub>2</sub>O<sub>5</sub>. *Acta Crystallogr., Sect. B: Struct. Crystallogr. Cryst. Chem.* **1971**, 27, 1476–1477.
- (36) Cocciantelli, J. M.; Doumerc, J. P.; Pouchard, M.; Broussely, M.; Labat, J. Crystal chemistry of electrochemically inserted  $\text{Li}_x \text{V}_2 \text{O}_5$ . *J. Power Sources* **1991**, 34, 103–111.
- (37) Cocciantelli, J. M.; Gravereau, P.; Doumerc, J. P.; Pouchard, M.; Hagenmuller, P. On the preparation and characterization of a new polymorph of  $V_2O_5$ . *J. Solid State Chem.* **1991**, *93*, 497–502.
- (38) Bish, D. L.; Howard, S. A. Quantitative Phase Analysis Using the Rietveld Method. *J. Appl. Crystallogr.* **1988**, *21*, 86–91.
- (39) Momma, K.; Izumi, F. VESTA 3for three-dimensional visualization of crystal, volumetric and morphology data. *J. Appl. Crystallogr.* **2011**, 44, 1272–1276.
- (40) Guo, Y.; Smith, R. B.; Yu, Z.; Efetov, D. K.; Wang, J.; Kim, P.; Bazant, M. Z.; Brus, L. E. Li Intercalation into Graphite: Direct Optical Imaging and Cahn-Hilliard Reaction Dynamics. *J. Phys. Chem. Lett.* **2016**, *7*, 2151–2156.
- (41) Stein, P.; Zhao, Y.; Xu, B.-X. Effects of Surface Tension and Electrochemical Reactions in Li-Ion Battery Electrode Nanoparticles. *J. Power Sources* **2016**, 332, 154–169.
- (42) Horrocks, G. A.; Braham, E. J.; Liang, Y.; De Jesus, L. R.; Jude, J.; Velázquez, J. M.; Prendergast, D.; Banerjee, S. Vanadium K-Edge X-ray Absorption Spectroscopy as a Probe of the Heterogeneous Lithiation of  $V_2O_5$ : First-Principles Modeling and Principal Component Analysis. *J. Phys. Chem. C* **2016**, 120, 23922–23932.
- (43) Satto, C.; Sciau, P.; Dooryhee, E.; Galy, J.; Millet, P. The  $\delta \rightarrow \varepsilon \rightarrow \gamma$ -LiV<sub>2</sub>O<sub>5</sub> "High Temperature" Phase Transitions Evidenced by Synchrotron X-Ray Powder Diffraction Analysis. *J. Solid State Chem.* **1999**, *146*, 103–109.
- (44) Galy, J.; Satto, C.; Sciau, P.; Millet, P. Atomic Modeling of the  $\delta\Leftrightarrow \varepsilon$  LiV<sub>2</sub>O<sub>5</sub> Phase Transition and Simulation of the XRD Powder Pattern Evolution. *J. Solid State Chem.* **1999**, *146*, 129–136.
- (45) Rozier, P.; Savariault, J. M.; Galy, J. A new interpretation of the  $\text{Li}_x \text{V}_2 \text{O}_5$  electrochemical behaviour for 1. *Solid State Ionics* **1997**, 98, 133–144.
- (46) Li, W.-D.; Xu, C.-Y.; Du, Y.; Fang, H.-T.; Feng, Y.-J.; Zhen, L. Electrochemical Lithium Insertion Behavior of  $\beta$ -Li<sub>x</sub>V<sub>2</sub>O<sub>5</sub> (0 <  $x \le 3$ ) as the Cathode Material for Secondary Lithium Batteries. *J. Electrochem. Soc.* **2014**, *161*, A75–A83.
- (47) Baddour-Hadjean, R.; Pereira-Ramos, J.-P. Raman Microspectrometry Applied to the Study of Electrode Materials for Lithium Batteries. *Chem. Rev.* **2010**, *110*, 1278–1319.
- (48) Baddour-Hadjean, R.; Marzouk, A.; Pereira-Ramos, J. P. Structural modifications of  $\text{Li}_x \text{V}_2 \text{O}_5$  in a composite cathode ( $0 \le x < 2$ ) investigated by Raman microspectrometry. *J. Raman Spectrosc.* **2012**, 43, 153–160.
- (49) Rey, I.; Lassègues, J. C.; Baudry, P.; Majastre, H. Study of a Lithium Battery by Confocal Raman Microspectrometry. *Electrochim. Acta* 1998, 43, 1539–1544.
- (50) Parija, A.; Liang, Y.; Andrews, J. L.; De Jesus, L. R.; Prendergast, D.; Banerjee, S. Topochemically De-Intercalated Phases of  $V_2O_5$  as Cathode Materials for Multivalent Intercalation Batteries: A First-Principles Evaluation. *Chem. Mater.* **2016**, 28, 5611–5620.
- (51) Parija, A.; Prendergast, D.; Banerjee, S. Evaluation of Multivalent Cation Insertion in Single- and Double-Layered Polymorphs of  $V_2O_5$ . ACS Appl. Mater. Interfaces **2017**, *9*, 23756–23765.
- (52) Carrasco, J. Role of van der Waals Forces in Thermodynamics and Kinetics of Layered Transition Metal Oxide Electrodes: Alkali and Alkaline-Earth Ion Insertion into  $V_2O_5$ . J. Phys. Chem. C **2014**, 118, 19599–19607.
- (53) Lozano, A.; Escribano, B.; Akhmatskaya, E.; Carrasco, J. Assessment of van der Waals Inclusive Density Functional Theory Methods for Layered Electroactive Materials. *Phys. Chem. Chem. Phys.* **2017**, *19*, 10133–10139.
- (54) Suthirakun, S.; Genest, A.; Rösch, N. Modeling Polaron-Coupled Li Cation Diffusion in  $V_2O_5$  Cathode Material. *J. Phys. Chem. C* **2018**, 122, 150–157.

- (55) Andrews, J. L.; Mukherjee, A.; Yoo, H. D.; Parija, A.; Marley, P. M.; Fakra, S.; Prendergast, D.; Cabana, J.; Klie, R. F.; Banerjee, S. Reversible Mg-Ion Insertion in a Metastable One-Dimensional Polymorph of V 2 O 5. *Chem* **2018**, *4*, 564–585.
- (56) Spitaler, J.; Sherman, E. Y.; Ambrosch-Draxl, C. First-Principles Study of Phonons, Optical Properties, and Raman Spectra in  $MgV_2O_5$ . *Phys. Rev. B: Condens. Matter Mater. Phys.* **2008**, 78, 064304.
- (57) Song, J.; Kim, J.; Kang, T.; Kim, D. Design of a Porous Cathode for Ultrahigh Performance of a Li-Ion Battery: An Overlooked Pore Distribution. *Sci. Rep.* **2017**, *7*, 42521.
- (58) Song, H.-M.; Yoo, D.-Y.; Hong, S.-K.; Kim, J.-S.; Cho, W. I.; Mho, S.-I. Electrochemical Impedance Analysis of  $V_2O_5$  and PEDOT Composite Film Cathodes. *Electroanalysis* **2011**, 23, 2094–2102.
- (59) Urquhart, S. G.; Hitchcock, A. P.; Smith, A. P.; Ade, H. W.; Lidy, W.; Rightor, E. G.; Mitchell, G. E. NEXAFS Spectromicroscopy of Polymers: Overview and Quantitative Analysis of Polyurethane Polymers. *J. Electron Spectrosc. Relat. Phenom.* 1999, 100, 119–135.
- (60) Ade, H.; Hitchcock, A. P. NEXAFS Microscopy and Resonant Scattering: Composition and Orientation Probed in Real and Reciprocal Space. *Polymer* **2008**, *49*, 643–675.
- (61) Maganas, D.; Roemelt, M.; Hävecker, M.; Trunschke, A.; Knop-Gericke, A.; Schlögl, R.; Neese, F. First principles calculations of the structure and V L-edge X-ray absorption spectra of  $V_2O_5$  using local pair natural orbital coupled cluster theory and spin-orbit coupled configuration interaction approaches. *Phys. Chem. Chem. Phys.* **2013**, 15, 7260–7276.
- (62) Goering, E.; Müller, O.; Klemm, M.; denBoer, M. L.; Horn, S. Angle dependent soft-X-ray absorption spectroscopy of  $V_2O_5$ . *Philos. Mag. B* **1997**, *75*, 229–236.
- (63) Velazquez, J. M.; Jaye, C.; Fischer, D. A.; Banerjee, S. Near Edge X-ray Absorption Fine Structure Spectroscopy Studies of Single-Crystalline  $\rm V_2O_5$  Nanowire Arrays. *J. Phys. Chem. C* **2009**, *113*, 7639–7645.
- (64) Horrocks, G. A.; De Jesus, L. R.; Andrews, J. L.; Banerjee, S. X-Ray Spectroscopy and Imaging as Multiscale Probes of Intercalation Phenomena in Cathode Materials. *JOM* **2017**, *69*, 1469–1477.
- (65) Patridge, C. J.; Jaye, C.; Abtew, T. A.; Ravel, B.; Fischer, D. A.; Marschilok, A. C.; Zhang, P.; Takeuchi, K. J.; Takeuchi, E. S.; Banerjee, S. An X-ray Absorption Spectroscopy Study of the Cathodic Discharge of Ag<sub>2</sub>VO<sub>2</sub>PO<sub>4</sub>: Geometric and Electronic Structure Characterization of Intermediate phases and Mechanistic Insights. *J. Phys. Chem. C* **2011**, *115*, 14437–14447.
- (66) Barai, P.; Huang, B.; Dillon, S. J.; Mukherjee, P. P. Mechano-Electrochemical Interaction Gives Rise to Strain Relaxation in Sn Electrochem. *J. Electrochem. Soc.* **2016**, *163*, A3022–A3035.
- (67) Barai, P.; Mukherjee, P. P. Mechano-Electrochemical Stochastics in High-Capacity Electrodes for Energy Storage. *J. Electrochem. Soc.* **2016**, *163*, A1120—A1137.